

Viscous effects on morphological and thermodynamic non-equilibrium characterizations of shock-bubble interaction

Dejia Zhang,^{1,2,3} Aiguo Xu,^{2,4,5, a)} Yanbiao Gan,⁶ Yudong Zhang,⁷ Jiahui Song,^{8,2,3} and Yingjun Li^{1, b)}

¹⁾State Key Laboratory for GeoMechanics and Deep Underground Engineering, China University of Mining and Technology, Beijing 100083, P.R.China

²⁾National Key Laboratory of Computational Physics, Institute of Applied Physics and Computational Mathematics, P. O. Box 8009-26, Beijing 100088, P.R.China

³⁾National Key Laboratory of Shock Wave and Detonation Physics, Mianyang 621000, China

⁴⁾HEDPS, Center for Applied Physics and Technology, and College of Engineering, Peking University, Beijing 100871, China

⁵⁾State Key Laboratory of Explosion Science and Technology, Beijing Institute of Technology, Beijing 100081, China

⁶⁾Hebei Key Laboratory of Trans-Media Aerial Underwater Vehicle, School of Liberal Arts and Sciences, North China Institute of Aerospace Engineering, Langfang 065000, China

⁷⁾School of Mechanics and Safety Engineering, Zhengzhou University, Zhengzhou 450001, P.R.China

⁸⁾School of Aerospace Engineering, Beijing Institute of Technology, Beijing, 100081, P.R.China

(Dated: 16 August 2023)

A two-fluid discrete Boltzmann model (DBM) with a flexible Prandtl number is formulated to study the shock-bubble interaction (SBI). This paper mainly focuses on the viscous effects on morphological and Thermodynamic Non-equilibrium (TNE) characterizations during the SBI process. Morphologically, viscosity affects the configuration of the vortex pair, increases both the gradients of density and temperature of the fluid field and reduces circulation of the bubble. As a higher viscosity fluid absorbs more energy from the shock wave, it leads to an increase in both the proportion of the high-density region and the corresponding boundary length for a fixed density threshold. The spatiotemporal features of TNE quantities are analyzed from multiple perspectives. The spatial configuration of these TNE quantities exhibit interesting symmetry, which aids in understanding the way and extent to which fluid unit deviating from equilibrium state. Theoretically, viscosity influences these TNE quantities by affecting the transport coefficient and gradients of macroscopic quantity. Meanwhile, the viscosity increases the entropy production rate originating from the non-organized momentum flux mainly through amplifying the transport coefficient, and enhances the entropy production rate contributed by the non-organized energy flux by raising the temperature gradient. These multi-perspective results collectively provide a relatively comprehensive depiction of the SBI.

I. Introduction

The physical scenarios of shock-bubble interaction (SBI) are ubiquitous in both natural phenomena and engineering applications.^{1–7} For example, in astrophysics, the Puppis A supernova remnant interacts with a complex system of interstellar clouds.⁸ In combustion systems, the shock wave ignites the mixture bubble composed of H_2 and O_2 .⁹ In inertial confinement fusion, the laser-induced shock wave impacts the isolated defects bubble inside the capsule, aggravating hydrodynamic instability.¹⁰ A fundamental setup for studying SBI involves a spherical bubble accelerated by a planar shock wave. Numerous physical factors influence the bubble deformation process, including the type and strength (Mach number, Ma) of the incident shock, the initial bubble shape, the boundary types of fluid field, the density ratio between the bubble and the ambient gas (Atwood number), the specific-heat ratio, the viscosity, and the heat conduction, etc. Given the significance of SBI in engineering applications, considerable efforts have been devoted

to unraveling its evolution mechanisms. Researchers have adopted various approaches, primarily encompassing theoretical methods,^{11,12} experimental investigations,^{2,13–15} and numerical simulations^{16–21}. Among these, Samtaney *et al.*¹¹ presented the analytical expressions for circulation Γ which are within and beyond the regular refraction regime. Ding *et al.*^{22,23} investigated experimentally and numerically the effects of initial interface curvature on the interaction between planar shock waves and heavy/light bubbles. Other scenarios, such as bubbles impacted by the converging shock wave,²⁴ spherical/cylindrical bubbles interact with planar shock wave under re-shock conditions,^{25,26} have also been investigated.

Numerical simulations of SBI are categorized into three types based on their theoretical foundation: macroscopic, mesoscopic, and microscopic methods. In previous studies, the traditional macroscopic modeling method, founded on the continuous hypothesis (or equilibrium and near-equilibrium hypothesis), has been widely employed. Such macroscopic fluid models are often represented by the Euler equations and Navier-Stokes (NS) equations, wherein the former assumes equilibrium, and the latter assumes near-equilibrium. The hydrodynamic equations in the traditional macroscopic modeling method only describe the hydrodynamic behaviors corresponding to the conservation laws of mass, momentum,

^{a)}Corresponding author: Xu_Aiguo@iapcm.ac.cn

^{b)}Corresponding author: lyj@aphy.iphy.ac.cn

and energy. However, with increasing the degree of non-equilibrium and non-continuity, more appropriate hydrodynamic equations refer to the Extended Hydrodynamic Equations (EHEs) encompass not only the evolution equations of conserved kinetic moments but also the most relevant non-conserved kinetic moments of the distribution function.²⁷ The traditional macroscopic model describes the SBI process from a macroscopic view mainly including the density, temperature, velocity, and pressure fields, providing much helpful and valuable physical research. For example, Ding *et al.*^{22,23} demonstrated a good agreement of interface structure between the numerical results obtained from the compressible Euler equations and experimental data. Zou *et al.*¹⁷ investigated the Atwood number effects and the jet phenomenon caused by the shock focusing through the multi-fluid Eulerian equations. In contrast, a smaller portion of SBI research utilizes the mesoscopic method, such as the Direct Simulation Monte Carlo method.²⁸

Two challenges are encountered in the previous SBI numerical studies. (i) Most of these studies describe mainly the flow morphology and SBI process from a macroscopic view. They are concerned more with dynamic processes such as bubble deformation, interface motion, vortex motion, mixing degree, etc. These physical quantities are helpful for understanding the flow morphology during the SBI process but are far from being sufficient. However, with increasing the non-continuity and Thermodynamic Non-Equilibrium (TNE), the complexity of system behaviors increases sharply. To ensure that the ability to describe the system does not decrease, more physical quantities such as the TNE quantities are needed to describe the state and behaviors. Many studies have emphasized the importance of investigating TNE behaviors for understanding the kinetic process.^{29–43} Among these, Zhang *et al.*⁴¹ studied the specific-heat ratio effects on kinetic processes of SBI from multiple perspectives. (ii) The viscous effects on small structures and kinetic features of SBI need further investigation. Research presented by Zhang *et al.*³⁹ has shown that viscosity plays an important role in material mixing in single-mode Rayleigh–Taylor (RT) system. Zhang *et al.*²⁸ demonstrated that the viscous effects lead to the disappearance of some typical phenomena on the reacting shock-bubble interaction. The bulk viscosity associated with the viscous excess normal stress, including different physical properties of diatomic and polyatomic gases, significantly changes the flow morphology and results in complex wave patterns, vorticity generation, vortex formation, and bubble deformation.⁴⁴ Moreover, studying the viscous effects on kinetic features, particularly on TNE features, is crucial for understanding the fundamental mechanism of viscous effects.

To further investigate the aforementioned inadequacies, we can employ the recently proposed discrete Boltzmann method/model/modeling (DBM).^{45,27,41,46–53} *The DBM serves as a physical modeling and the analysis method of complex physical field.* Its tasks mainly include two aspects: (i) Capturing the main features of the problems to be studied. In addition to mass, momentum, and energy conservation moments, the DBM considered more relevant non-conserved kinetic moments that describe the main TNE behaviors of the system.

With the increase of TNE, more non-conserved kinetic moments should be required to ensure the non-significant decrease of the system state and behavior description function. Through the Chapman-Enskog (CE) multiscale analysis, the kinetic moments describe the system state and features can be quickly determined. It should be noted that, for complex systems, each kinetic moment represents one perspective and complex systems require multi-perspective research. The result from these perspectives together constitutes a relatively complete description of the system. (ii) Trying to extract more valuable physical information for massive data and complex physical fields. Based on the non-equilibrium statistical physics, the DBM uses the non-conservative moments of $(f - f^{eq})$, i.e., the TNE quantities, to describe how and how much the system deviates from the thermodynamic equilibrium state and to check corresponding effects due to deviating from the thermodynamic equilibrium.⁴⁶ The TNE quantities open a high-dimensional phase space, and this phase space and its sub-space provide an intuitive geometric correspondence for grasping complex behaviors. Many kinds of TNE quantities can be defined according to the research requirement, and each TNE characteristic quantity describes the TNE behaviors from its own perspective. Other analysis methods such as the morphological analysis method based on the Minkowski measures,⁵⁴ and the description of tracer particle method,³⁹ are also coupled in DBM. These analysis methods constitute a relatively complete description for complex physical field. Summarily, DBM modeling surpasses the traditional macroscopic modeling in at least two aspects: (i) the extension of description ability for non-equilibrium flows. The physical function of DBM corresponds to the EHEs which considers not only the evolution of conserved kinetic moments, but also the evolution of non-conserved moments. That enables the DBM to describe the higher TNE flows more accurate. (ii) DBM also provides a set of analysis methods for complex physical field. In numerical simulation research, NS is only responsible for physical modeling before simulation and not for the analysis of the complex physical field after simulation; While the DBM is responsible for both pre simulation and post simulation.

In the following part, Section II presents the physical modeling process which includes the coarse-grained modeling that describes the SBI process and the TNE analysis scheme extracted the information from the complex physical field. Section III shows the numerical results and Sec. IV concludes this paper.

II. Physical model construction

A first-order two-fluid DBM with a flexible Prandtl (Pr) number is used to describe the SBI process in this paper, where “first-order” means only the first order of TNEs are considered in the modeling process. From the original Boltzmann equation to a first-order two-fluid DBM, four physical steps are needed. (i) Simplifying and modifying the Boltzmann equation according to the physical requirement. (ii) Discretizing the particle velocity space. (iii) Checking the TNE

state and extracting TNE information. (iv) Selecting and designing a proper boundary condition. Among these, steps (i) and (ii) contain the two physical constraints in coarse-grained modeling of DBM, respectively.

A. Simplifying and modifying the Boltzmann equation

To facilitate the solution of the Boltzmann equation, the original complex collision operator should be simplified. In this step, it requires that the physical quantities described the physical problems cannot be changed before and after simplification, i.e., $\int Q(f, f') \Psi(\mathbf{v}) d\mathbf{v} = \int -\frac{1}{\tau} (f - f^{eq}) \Psi(\mathbf{v}) d\mathbf{v}$, where $\Psi = [1, \mathbf{v}, \mathbf{v}\mathbf{v}, \mathbf{v}\mathbf{v}\mathbf{v}, \dots]^T$ represents the concerned kinetic moments. To realize a adjustable Pr number, the Ellipsoidal Statistical Bhatnagar-Gross-Krook (ES-BGK) Boltzmann equation is adopted in this work^{49,55,56}. The Boltzmann equation in ES-BGK form is

$$\frac{\partial f}{\partial t} + \mathbf{v} \cdot \frac{\partial f}{\partial \mathbf{r}} = -\frac{1}{\tau} (f - f^{ES}), \quad (1)$$

where \mathbf{v} , \mathbf{r} , t , and τ represent the particle velocity, particle position, time, and relaxation time, respectively. The ES distribution function f^{ES} is

$$f^{ES} = \frac{\rho}{2\pi\sqrt{|\lambda_{\alpha\beta}|}} \times \exp\left[-\frac{1}{2}\lambda_{\alpha\beta}^{-1}(\mathbf{v}_\alpha - \mathbf{u}_\alpha)(\mathbf{v}_\beta - \mathbf{u}_\beta)\right], \quad (2)$$

where ρ is the mass density and \mathbf{u}_α (\mathbf{u}_β) represents the flow velocity in α (β) ($\alpha, \beta = x$ or y) direction. The modified term is $\lambda_{\alpha\beta} = RT\delta_{\alpha\beta} + \frac{b}{\rho}\Delta_{2,\alpha\beta}^*$, with b a flexible parameter adjusting the Pr number, i.e., $\text{Pr} = 1/(1 - b)$. When $b = 0$, f^{ES} is reduced to f^{eq} and the ES-BGK form is simplified to the BGK form.

B. Discretizing the particle velocity space and determining the physical requirement for two-fluid system

For simulation, the continuous Boltzmann equation should be discretized in its velocity space. In this step, the continuous kinetic moments should be transferred into summation form. So the reserved kinetic moments need to keep their values after discretizing the velocity space, i.e., $\int f \Psi'(\mathbf{v}) d\mathbf{v} = \sum_i f_i \Psi'(\mathbf{v}_i)$. Because the distribution function f can be expressed by f^{eq} , so the reserved kinetic moments of f^{eq} should keep their values, i.e., $\int f^{eq} \Psi''(\mathbf{v}) d\mathbf{v} = \sum_i f_i^{eq} \Psi''(\mathbf{v}_i)$, where Ψ' and Ψ'' represent the conserved kinetic moments. The conserved kinetic moments depend on specific physical problems. In DBM, the CE analysis is used to determine conserved kinetic moments. Specifically, five kinetic moments are determined when constructing a first-order DBM, i.e., \mathbf{M}_0^{ES} , \mathbf{M}_1^{ES} , \mathbf{M}_2^{ES} , \mathbf{M}_3^{ES} , $\mathbf{M}_{4,2}^{ES}$. Their expressions are shown in the Appendix A. They can be obtained by integrating the Eq. (3) in the particle velocity space \mathbf{v} . Because the f^{ES} relates to $\Delta_{2,\alpha\beta}^*$, so it also needs the kinetic moments of f^{eq} in modeling process, i.e., \mathbf{M}_0^{eq} , \mathbf{M}_1^{eq} , \mathbf{M}_2^{eq} , \mathbf{M}_3^{eq} , $\mathbf{M}_{4,2}^{eq}$. Their expressions

can be obtained by submitting $b = 0$ into \mathbf{M}_m^{ES} ($\mathbf{M}_{m,n}^{ES}$). For convinence, we can write the kinetic moments into a matrix equation*, i.e.,

$$\mathbf{C} \cdot \mathbf{f}^{\sigma,ES} = \hat{\mathbf{f}}^{\sigma,ES}, \quad (3)$$

and

$$\mathbf{C} \cdot \mathbf{f}^{\sigma,eq} = \hat{\mathbf{f}}^{\sigma,eq}, \quad (4)$$

Equations (3) and (4) are exactly the physical constraints given by the second step in DBM modeling. According to the number of the reserved kinetic moment, the dimension of $\hat{\mathbf{f}}^{\sigma,eq}$ ($\hat{\mathbf{f}}^{\sigma,ES}$) is $\hat{\mathbf{f}}^{\sigma,eq} = (\hat{f}_1^{\sigma,eq}, \hat{f}_2^{\sigma,eq}, \dots, \hat{f}_{N_{\text{moment}}}^{\sigma,eq})^T$ [$\hat{\mathbf{f}}^{\sigma,ES} = (\hat{f}_1^{\sigma,ES}, \hat{f}_2^{\sigma,ES}, \dots, \hat{f}_{N_{\text{moment}}}^{\sigma,ES})^T$], with $N_{\text{moment}} = 13$. \mathbf{C} represents the matrix of discrete velocity model (DVM). It should be noted that the DBM retains the use of discrete velocities, but does not adhere to the specific discrete format, only gives the most necessary physical constraints for the discrete velocities selection to follow. In brief, the DBM provides the necessary physical constraints that should be obeyed during the discretization of particle velocity space.

To describe the interaction between two different fluid components, we should introduce two sets of distribution functions. Each distribution function describes one fluid component, and it corresponds to one sets of hydrodynamic quantities (density ρ^σ , flow velocity \mathbf{u}^σ , temperature T^σ , pressure p^σ). After this step, the two-fluid discrete Boltzmann equation in ES-BGK form can be obtained, i.e.,

$$\frac{\partial f_i^\sigma}{\partial t} + \mathbf{v}_{i\alpha} \cdot \frac{\partial f_i^\sigma}{\partial \mathbf{r}_\alpha} = -\frac{1}{\tau^\sigma} (f_i^\sigma - f_i^{\sigma,ES}), \quad (5)$$

where the superscript σ represents the type of fluid component, i.e., $\sigma = A$ or B . The i is the kind of discrete velocities. The relaxation time τ^σ relates to the mass particle density ρ^σ and the flexible parameter θ^σ , i.e., $\tau^\sigma = 1/(\rho^A/\theta^A + \rho^B/\theta^B)$. $f^{\sigma,ES} = f^{\sigma,ES}(\rho^\sigma, \mathbf{u}, T)$, with ρ^σ , \mathbf{u} , T are the mass density of component σ , flow velocity of mixture, temperature of mixture, respectively. In two-fluid DBM, the mass density and flow velocity of each component are calculated by the first two conserved kinetic moments, respectively, i.e.,

$$\rho^\sigma = \sum_i f_i^\sigma, \quad (6)$$

$$\mathbf{u}^\sigma = \frac{\sum_i f_i^\sigma \mathbf{v}_i}{\rho^\sigma}, \quad (7)$$

The mass density and flow velocity of mixture are

$$\rho = \sum_\sigma \rho^\sigma, \quad (8)$$

$$\mathbf{u} = \frac{\sum_\sigma \rho^\sigma \mathbf{u}^\sigma}{\rho}, \quad (9)$$

The temperature of each component and mixture are obtained from the third conserved kinetic moment

$$T^{\sigma*} = \frac{2E_f^{\sigma*}}{D\rho^\sigma}, \quad (10)$$

$$T = \frac{2E_I^*}{\sum_{\sigma} D \rho^{\sigma}}, \quad (11)$$

where $E_I^* = \sum_{\sigma} E_I^{\sigma*}$ and $E_I^{\sigma*} = \frac{1}{2} \sum_i f_i^{\sigma} (\mathbf{v}_i - \mathbf{u})^2$ is the internal energy of component σ . D represents the spatial dimension.

According to the CE multiscale analysis, the Boltzmann equation can be reduced to the macroscopic hydrodynamic equations (see the Appendix B). It should be noted that recovering the corresponding hydrodynamic equations is only one part of the physical function of DBM. Physically, the physical function of DBM corresponds to the EHEs which not only reserve the conserved kinetic moments evolution equations, but also some of the most closely related non-conserved moments evolution equations. We refer the modeling method which derives EHEs from the Boltzmann equation to Kinetic Macroscopic Modeling (KMM) method. However, the DBM is a kind of Kinetic Direct Modeling (KDM) method. In DBM, deriving the hydrodynamic equations is used to verify the correctness of physical modeling, the DBM does not need to solve the hydrodynamic equations.

C. Checking the TNE state and extracting TNE information

In DBM, the non-conserved kinetic moments reflect the way and degree of the systems deviating from thermodynamic equilibrium. By analyzing the non-conservative moments of $(f - f^{eq})$, we can effectively characterize the TNE state and extract valuable TNE information from the fluid system. Because the DBM used in this paper only considered a limited number of non-conserved kinetic moments, it only captures parts of the TNE behaviors of non-equilibrium systems. However, these captured TNE behaviors are the most relevant and critical parts for understanding the system's overall dynamics and characteristics.

In a first-order DBM, four fundamental TNE quantities can be defined, i.e., $\Delta_2^{\sigma*}$, $\Delta_{3,1}^{\sigma*}$, $\Delta_3^{\sigma*}$, and $\Delta_{4,2}^{\sigma*}$. Their definitions are:

$$\Delta_m^{\sigma*} = \sum_i (f_i^{\sigma} - f_i^{\sigma,eq}) \underbrace{\mathbf{v}_i^* \mathbf{v}_i^* \cdots \mathbf{v}_i^*}_m, \quad (12)$$

$$\Delta_{m,n}^{\sigma*} = \frac{1}{2} \sum_i (f_i^{\sigma} - f_i^{\sigma,eq}) (\mathbf{v}_i^* \cdot \mathbf{v}_i^*)^{(m-n)/2} \underbrace{\mathbf{v}_i^* \cdots \mathbf{v}_i^*}_n, \quad (13)$$

where $\mathbf{v}_i^* = \mathbf{v}_i - \mathbf{u}$ represents the central velocity, with \mathbf{u} the macro flow velocity. The subscript “ m, n ” means that the m -order tensor is contracted to n -order tensor. The first two, $\Delta_2^{\sigma*} = \Delta_{2,\alpha\beta}^{\sigma*} \mathbf{e}_{\alpha} \mathbf{e}_{\beta}$ and $\Delta_{3,1}^{\sigma*} = \Delta_{3,1,\alpha}^{\sigma*} \mathbf{e}_{\alpha}$, are the most typical TNE quantities, where \mathbf{e}_{α} (\mathbf{e}_{β}) is the unit vector in the α (β) direction. Physically, they correspond to more generalized viscous stress (or non-organized momentum flux, NOMF) and heat flux (or non-organized energy flux, NOEF), respectively. The latter two TNE quantities contain condensed information. The $\Delta_3^{\sigma*}$ ($\Delta_{4,2}^{\sigma*}$) represents the more generalized flux of $\Delta_2^{\sigma*}$

($\Delta_{3,1}^{\sigma*}$). The spatiotemporal evolution of these four TNE quantities is a common scheme that described the way and degree of fluid unit deviating from the equilibrium state.

In addition, other coarse-grained TNE quantities can be defined. For example, integrating and rooting the independent components of each above TNE quantity, the average TNE strength described by the degree of each fluid unit deviating from equilibrium is obtained, i.e.,

$$|\Delta_2^{\sigma*}| = \sqrt{\Delta_{2,xx}^{\sigma*2} + 2\Delta_{2,xy}^{\sigma*2} + \Delta_{2,yy}^{\sigma*2}}, \quad (14)$$

$$|\Delta_{3,1}^{\sigma*}| = \sqrt{\Delta_{3,1,x}^{\sigma*2} + \Delta_{3,1,y}^{\sigma*2}}, \quad (15)$$

$$|\Delta_3^{\sigma*}| = \sqrt{\Delta_{3,xxx}^{\sigma*2} + 3\Delta_{3,xyx}^{\sigma*2} + 3\Delta_{3,xyy}^{\sigma*2} + \Delta_{3,yyy}^{\sigma*2}}, \quad (16)$$

$$|\Delta_{4,2}^{\sigma*}| = \sqrt{\Delta_{4,2,xx}^{\sigma*2} + 2\Delta_{4,2,xy}^{\sigma*2} + \Delta_{4,2,yy}^{\sigma*2}}, \quad (17)$$

where the operator “ $|\cdot|$ ” indicates summing all the components. Further, summing their non-dimensional values over the whole fluid field, the total TNE strength described the fluid system can be obtained, i.e., $d_2^{\sigma*} = \sum_{ix,iy} |\Delta_2^{\sigma*2}/T^2|$,

$d_3^{\sigma*} = \sum_{ix,iy} |\Delta_3^{\sigma*2}/T^3|$, $d_{3,1}^{\sigma*} = \sum_{ix,iy} |\Delta_{3,1}^{\sigma*2}/T^3|$, and $d_{4,2}^{\sigma*} = \sum_{ix,iy} |\Delta_{4,2}^{\sigma*2}/T^4|$, where “ ix ” and “ iy ” represent the positions of fluid unit. In addition, summing the four non-dimensional TNE quantities, another total TNE strength quantity, which contains more condensed information, can also be defined, i.e.,

$$d^{\sigma*} = \sum_{ix,iy} \sqrt{|\frac{\Delta_2^{\sigma*2}}{T^2}| + |\frac{\Delta_{3,1}^{\sigma*2}}{T^3}| + |\frac{\Delta_3^{\sigma*2}}{T^3}| + |\frac{\Delta_{4,2}^{\sigma*2}}{T^4}|}. \quad (18)$$

It should be noticed that these TNE quantities describe the TNE behaviors from their own perspectives. The fluid system needs multi-perspective research. The results from multi-perspective together constitute a relatively complete description of the system. In brief, the DBM provides the most relevant TNE effects which are not convenient to obtain from NS model.

III. Numerical simulations and results

A. Selecting the discrete scheme

To obtain the values of $f_i^{\sigma,eq}$ and $f_i^{\sigma,ES}$, we must select a specific DVM, i.e., the matrix \mathbf{C} in Eqs. (3) and (4). The selection of DVM must obey the physical constrain given by the reserved kinetic moments. Thus, the dimension of \mathbf{C} is $\mathbf{C} = (\mathbf{c}_1, \mathbf{c}_2, \cdots, \mathbf{c}_{N_i})$, with $\mathbf{c}_i = (1, v_{ix}, v_{iy}, \cdots, \frac{1}{2}v_{iy}^2 v_{ix}^2)^T$, and N_i the number of discrete velocities. The selection of

C also considers the numerical stability and computational efficiency, etc. Once a specific DVM determined, the values of $f_i^{\sigma,eq}$ can be obtained, i.e., $\mathbf{f}^{\sigma,eq} = \mathbf{C}^{-1} \cdot \hat{\mathbf{f}}^{\sigma,eq}$, where \mathbf{C}^{-1} is the inverse matrix of **C**. Calculating the values of $\Delta_{2,\alpha\beta}^*$, and submitting they into $\hat{\mathbf{f}}^{\sigma,ES}$, we can get $f_i^{\sigma,ES}$, i.e., $\mathbf{f}^{\sigma,ES} = \mathbf{C}^{-1} \cdot \hat{\mathbf{f}}^{\sigma,ES}$. It should be noticed that solving the inverse matrix is one of the common ways to obtain $\mathbf{f}^{\sigma,eq}$, but is not the standard or the best method. The number of discrete velocity is chosen to be equal to the number of kinetic moment in this paper, i.e., $N_i = N_{\text{moment}}$. We can choose the D2V13 model in this paper, its sketches can be seen in Fig. 1. The specific values of D2V13 are given as:

$$(v_{ix}, v_{iy}) = \begin{cases} c_1 [\cos \frac{(i-1)2\pi}{3}, \sin \frac{(i-1)2\pi}{3}], & i = 1-3, \\ c_2 [\cos \frac{(i-4)2\pi}{5}, \sin \frac{(i-4)2\pi}{5}], & i = 4-8, \\ c_3 [\cos \frac{(i-9)2\pi}{5}, \sin \frac{(i-9)2\pi}{5}], & i = 9-13, \end{cases}$$

where c_1 , c_2 and c_3 are adjustable parameters of the DVM. Then, it is very convenient to get \mathbf{C}^{-1} through some mathematical software such as Mathematica, etc.

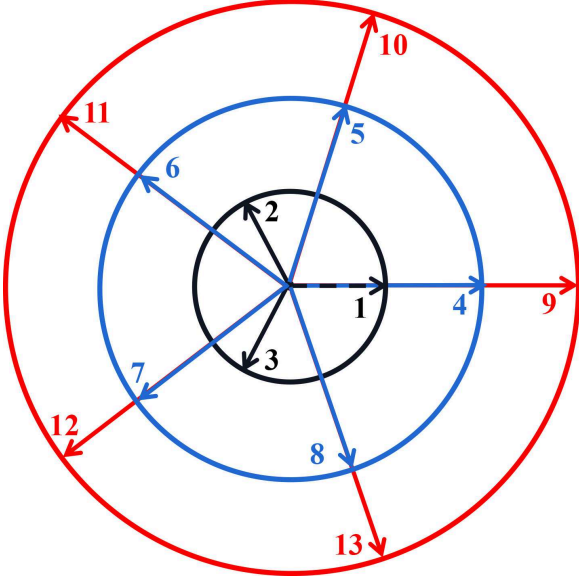


FIG. 1. Sketch of the D2V13 model.

Actually, the standard Lattice Boltzmann Method (LBM) inherits a physical image of “propagation + collision” in a given way of “virtual particle”.^{57,58} The direction of discrete velocity represents the motion direction of these “virtual particle”. This concise image is beneficial for improving the computation efficiency of LBM. However, there is no this image in DBM. Although DBM retains the use of discrete velocity, the direction of discrete velocity in DBM does not indicates the motion direction of particles. The function of DVM in DBM is to keep the values of the reserved kinetic moments. The specific discrete formats for the spatial derivative, time integral and discrete velocities should be selected reasonably according to the specific situation. The specific discrete format presented in this paper is only a set of choices based on

a series of attempts to meet the current research needs, and is by no means a standard or optimal template. In this paper, the first-order forward Euler finite difference scheme and the second-order non-oscillatory non-free dissipative scheme are used to solve the two partial derivatives in Eq. (5), respectively.

B. Configuration and initial conditions

Figure 2 illustrates the configuration of the interaction between a planar shock wave and a cylindrical bubble. The flow field is rectangular with a dimensionless scale of $L_x \times L_y = 0.24 \times 0.12$, where the left side corresponds to the high-pressure region, and the right area is the lower-pressure region. It is divided into $N_x \times N_y = 800 \times 400$ grid size. After the initial moment, a planar shock wave with a strength of $\text{Ma} = 1.23$ propagates downstream and impacts the high-density bubble. The initial macroscopic conditions of the flow field are as follows:

$$\begin{cases} (\rho, T, u_x, u_y)_{\text{bubble}} = (5.0168, 1.0, 0.0, 0.0), \\ (\rho, T, u_x, u_y)_1 = (1.29201, 1.303295, 0.393144, 0.0), \\ (\rho, T, u_x, u_y)_0 = (1.0, 1.0, 0.0, 0.0), \end{cases}$$

where the subscript “0” (“1”) represents the low-pressure (high-pressure) region. Other parameters used for the simulation are: $c_1 = 0.8$, $c_2 = 1.6$, $c_3 = 2.4$, $\Delta x = \Delta y = 3 \times 10^{-4}$, $\Delta t = 1 \times 10^{-6}$, $\theta^A = \theta^B = 4 \times 10^{-6}$. The left (right) side of the flow field uses the inflow (outflow) boundary condition. The periodic boundary is adopted in the y direction. To study the viscous effects on SBI, we vary the viscosity coefficient of the bubble by adjusting the Pr number. Fives cases with different Pr numbers are simulated in this work, i.e., $\text{Pr} = 1.0, 1.25, 2.0, 3.33$, and 10.0 . The larger the Pr number, the larger the viscosity coefficient (the viscosity formula in ES-BGK DBM can be seen in the Appendix B).

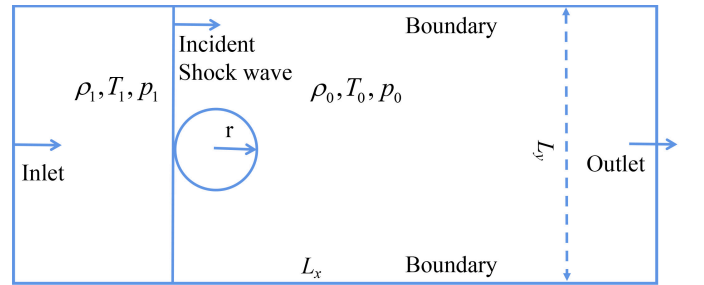


FIG. 2. The computational configuration of the SBI.

C. Morphological features

Shown in Fig. 3 are the density contours (left column) and schlieren images (right column) at five different moments, with $\text{Pr} = 1.0$. There are mainly two stages for SBI, i.e., the shock compression stage ($t < 0.05$) and the post-shock

stage ($t > 0.05$). At $t = 0$, the incident shock impacts the bubble interface, resulting in the generation of a downstream-traveling transmitted shock (TS) and an upward-moving reflected shock (RS) due to the refraction of the shock wave, as depicted in $t = 0.02$. This stage is characterized by the misalignment between the density gradient and pressure gradient, leading to the vorticity deposition effect, which is the intrinsic mechanism behind the formation of two pairs of vortex rings. Afterward, as TSs move downstream, they would converge near the downstream pole, causing the shock focusing and the generation the jet structure. Subsequently, due to the deposited vorticity, a pair of counter-rotating vortexes produces. Figure 4 plots the density contours at three moments with for cases with five different Pr numbers (different viscosities). It can be seen that until $t = 0.05$, there are almost no differences among cases with different viscosities because the viscous effects are relatively weaker compared to the shock compression effects. However, at the post-shock stage, the viscous effects are gradually becoming apparent. The discernable difference (marked by the red circles in the figures) around the undeveloped vortex pair can be observed at $t = 0.15$. The undeveloped vortex pair in case with a higher viscosity is smaller. As the vortexes continue to develop, the influence of viscosity on their shape becomes significantly more pronounced.

To further investigate the viscous effects on macroscopic fluid fields, we analyze the density and temperature fields along the y axis by summing $\rho(x, y)$ and $T(x, y)$ (i.e., $\sum_y \rho(x, y)$ and $\sum_y T(x, y)$), and obtain their corresponding gradients (i.e., $\nabla_x \rho_s$ and $\nabla_x T_s$, where $\rho_s = \sum_y \rho(x, y)$ and $T_s = \sum_y T(x, y)$). As shown in Figs. 5(a) and (b), profiles of $\nabla_x \rho_s$ and $\nabla_x T_s$ at two different moments are plotted, respectively. At $t = 0.02$, there are no obvious differences between cases with different viscosities for both gradients of density and temperature. However, some discernible differences can be observed in the corresponding sub-figures, indicating that cases with higher viscosity exhibit larger peaks. At $t = 0.4$, the differences between cases with different viscosities become more visible. It also can be seen that the viscosity increases both the density and temperature gradients. The reason relates to that the higher-viscosity fluid is easier to absorb energy from shock wave. To investigate the viscous effects on the velocity field, Fig. 5(c) plots the temporal evolution of bubble circulation during the SBI process. $\Gamma^+ = \sum \omega|_{\omega>0} \Delta x \Delta y$ ($\Gamma^- = \sum \omega|_{\omega<0} \Delta x \Delta y$) means the positive (negative) circulation and $\Gamma = \sum \omega \Delta x \Delta y$ represents the total circulation, where $\omega = (\partial u_y / \partial x - \partial u_x / \partial y) \mathbf{e}_z$ is the vorticity. The circulation can be used to describe the strengths of vorticity and velocity shear effect. During the shock compression stage, the circulations increase rapidly due to the vorticity deposition effect. In this stage, the viscosity contributes little effect to circulations. However, as the shock wave sweeps through the bubble and the vortex pair continuously develops, its influences are gradually apparent, i.e., the viscosity reduces the values of circulation. It indicates that the viscosity inhibits the shear motion of the bubble.

The utilization of Minkowski measures is an effective method to extract information from complex physical field.^{29,34,54,59} It provides a complete description for a Tur-

ing pattern. In a D -dimensional space, a set of convex sets that satisfy motion invariance and additivity can be fully described by $D + 1$ Minkowski measures. In a two-dimensional case, the three Minkowski measures include the proportion A of the high- Θ region (i.e., $A = A_h / A_{total}$, where A_h is the area of high- Θ region and A_{total} is the area of fluid field), the boundary length L between the high- and low- Θ regions, and the Euler characteristic χ , where Θ can refer to density, temperature, velocity, or pressure.

In the following analysis, we focus on density Turing patterns (i.e., Θ is density). Fig. 6 investigates the viscous effects on the proportion A and boundary length L of density Turing patterns, where “th” indicates the “threshold” value. The selection of the threshold value depends on the specific physical effects to be considered. For example, when $\rho_{th} > \rho_0$ (where $\rho_0 = 5.0168$ is the initial density of the bubble), the proportion A and boundary length L reflect the abilities of viscosity to achieve a high-density state due to the shock compression. When $\rho_{th} < \rho_0$, the viscous effects on bubble deformation and diffusion which result in a lower density, has also been taken into account. In Fig. 6(a), for cases $\rho_{th} = 0.01$ and $\rho_{th} = 0.5$, the proportion A decreases rapidly during the incident shock acting on the bubble. After the shock sweeps through the bubble, the proportion A gradually increases due to the bubble deformation and gas diffusion effects. During the earlier stage, the viscosity has little impact on the proportion A because shock compression dominates. However, in the later stage, the viscosity noticeably reduces the values of proportion A due to its adverse effect on deformation. When $\rho_{th} = 5.5$, the values of proportion A increase from zero due to the shock compression, and then decrease slowly because of the deformation and diffusion. When further increasing the ρ_{th} , the high-density region only appears around $t = 0.05$ and almost disappears at other times. In contrast to cases with $\rho_{th} < \rho_0$, in cases $\rho_{th} > \rho_0$, the viscosity increases the proportion A . Overall, the viscosity reduces the lower- ρ_{th} region but increases the higher- ρ_{th} region. The reason is that the fluid with a higher viscosity can absorb more energy from shock wave, making it easier to increase the density during the compression process. Fig. 6 (b) shows the temporal evolution of boundary length L . Similar to the proportion A , the viscous effects are more significant in the later stage. In addition, the viscosity reduces the boundary length L for cases with $\rho_{th} = 0.01$ and $\rho_{th} = 0.5$, but increases it for cases with $\rho_{th} = 5.5$ and $\rho_{th} = 7.5$.

D. TNE features

Understanding the spatial and temporal evolutions of TNE quantities is crucial for further investigating the kinetic behaviors during the SBI process. To provide an intuitive representation of TNE quantities, Fig. 7 plots the contours of two fundamental TNE quantities at three different moments. In this figure, the odd and even rows represent TNE quantities of component A and B , respectively. Among these, the first and last two rows correspond $|\Delta_2^{\sigma*}|$ and $|\Delta_{3,1}^{\sigma*}|$, respectively. It can be seen that the values of $|\Delta_2^{\sigma*}|$ and $|\Delta_{3,1}^{\sigma*}|$ are greater than zero in regions where the gradients of macroscopic quan-

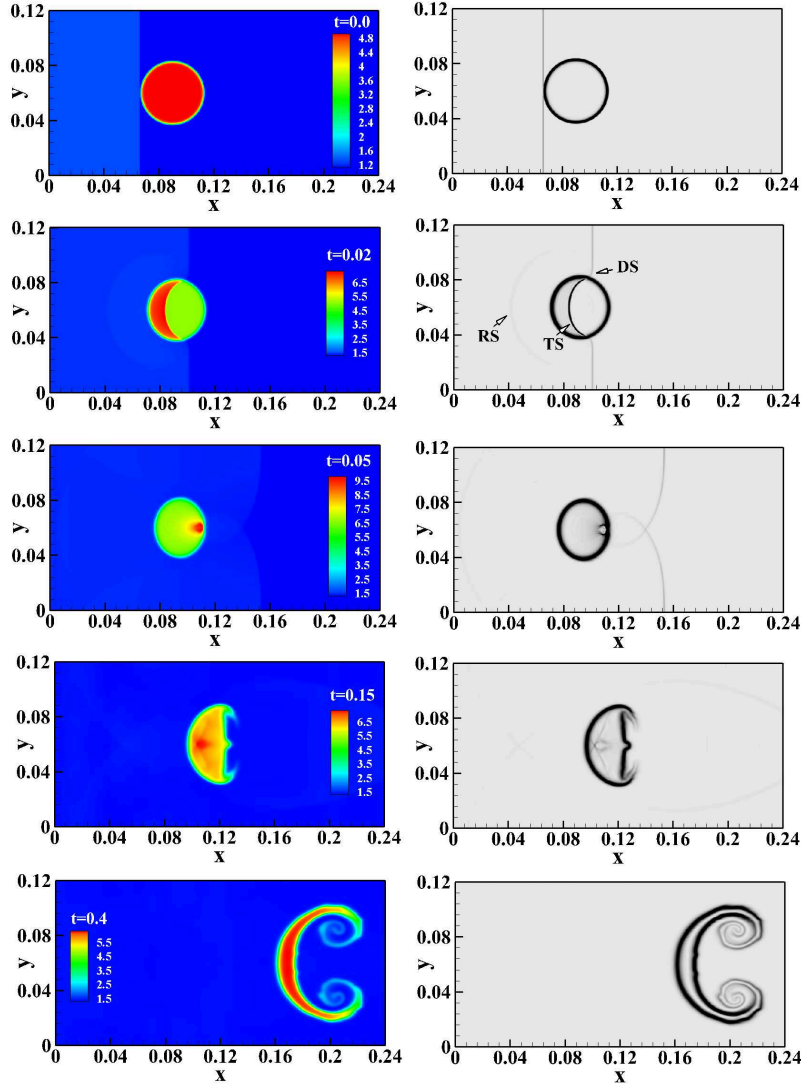


FIG. 3. Density contours (left column) and schlieren images (right column) at five different moments.

tities are pronounced, indicating significant deviations from the thermodynamic equilibrium state. The larger the value of the TNE quantity, the higher the degree of deviation from the thermodynamic equilibrium state.

To qualitatively investigate the viscous effects on the spatial evolution of TNE quantities, two physical quantities ($\overline{\Delta_{2,\alpha\beta}^{\sigma*}} = \sum_x \Delta_{2,\alpha\beta}^{\sigma*} / N_x$ and $\overline{\Delta_{3,1,\alpha}^{\sigma*}} = \sum_x \Delta_{3,1,\alpha}^{\sigma*} / N_x$), are defined to describe the TNE strength of each row of the fluid field. Shown in Figs. 8(a)-(d) are the profiles of $\overline{\Delta_{2,\alpha\beta}^{A*}}$, $\overline{\Delta_{2,\alpha\beta}^{B*}}$, $\overline{\Delta_{3,1,\alpha}^{A*}}$, and $\overline{\Delta_{3,1,\alpha}^{B*}}$ at moment $t = 0.02$, respectively. Different symbols indicate cases with various viscosities. It is evident that the values of TNE quantities around the contact interface are relatively larger and the profiles of these TNE quantities show obvious symmetry. Actually, these TNE quantities describe the TNE behaviors from their own perspectives. Specifically, Fig. 8(a) shows the view of $\overline{\Delta_{2,\alpha\beta}^{\sigma*}}$. Clearly, $\overline{\Delta_{2,\alpha\beta}^{A*}}$ is symmetric about the central line $y = 0.6$, indicating that the upper

and lower parts of the fluid field deviate from the thermodynamic equilibrium state in the same direction, and with the same amplitude. The profile of $\overline{\Delta_{2,\alpha\beta}^{A*}}$ is also symmetric about the central line $y = 0.6$. In addition, $\overline{\Delta_{2,\alpha\beta}^{A*}}$ and $\overline{\Delta_{2,\alpha\beta}^{B*}}$ are symmetric about the line $\overline{\Delta_{2,\alpha\beta}^{A*}} = 0$, which means that looking at the TNE strength of each fluid unit from these two perspectives yields opposite results. What can also be seen is that $\overline{\Delta_{2,\alpha\beta}^{A*}}$ is symmetry about the origin point. It indicates that the upper and lower parts of the flow field deviate from equilibrium in opposite directions, but deviate with the same amplitude. What's more, the viscosity has not too many influences on $\overline{\Delta_{2,\alpha\beta}^{A*}}$, except some differences around the contact interface. The reason is that, at moment $t = 0.02$, when changing the Pr number of component B, the resulting changes of the macroscopic flow field of component A are relatively smaller. As shown in Fig. 8(b), the $\overline{\Delta_{2,\alpha\beta}^{B*}}$ and $\overline{\Delta_{2,\alpha\beta}^{A*}}$ are also symmetric

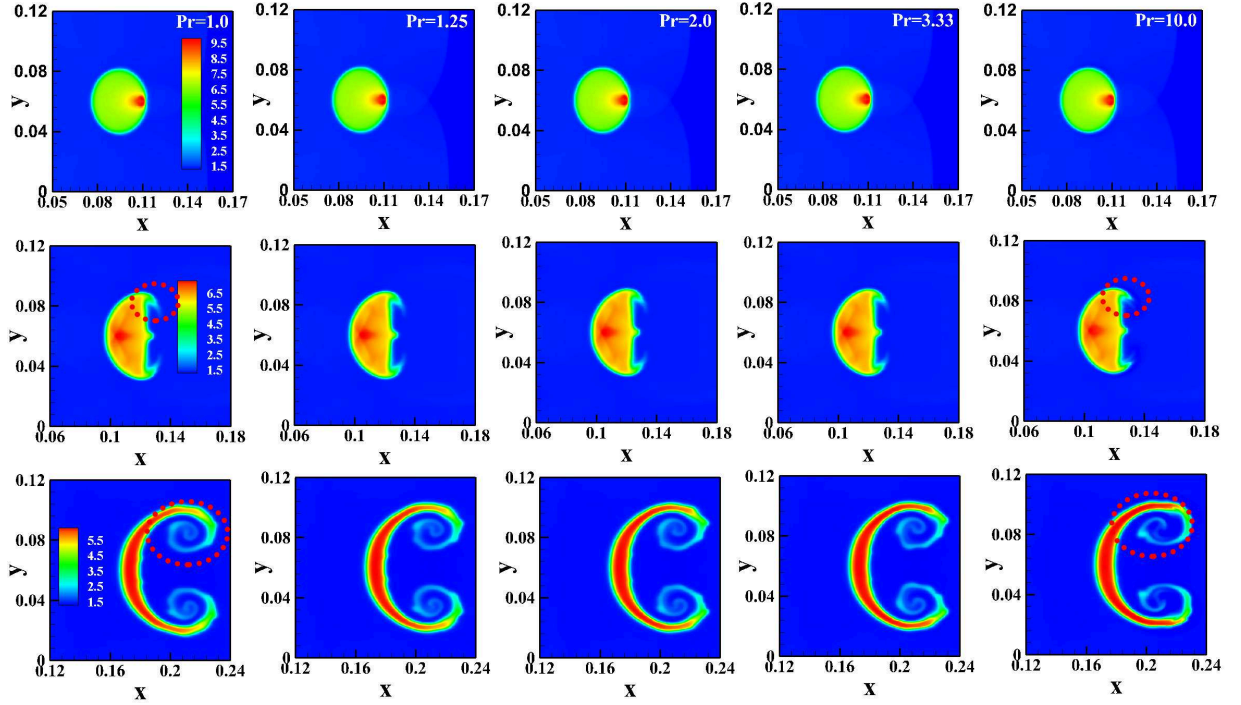


FIG. 4. Density contours at $t = 0.05$ (first row), $t = 0.15$ (second row) and $t = 0.42$ (third row), with different Pr numbers (different viscosities).

about the line $\overline{\Delta_{2,\alpha\beta}^{B*}} = 0$. The $\overline{\Delta_{2,xy}^{B*}}$ is also symmetry about the origin point. Obviously, the Pr number influences significantly the values of $\overline{\Delta_{2,\alpha\beta}^{B*}}$. Higher Pr numbers of component B result in larger deviations from the thermodynamic equilibrium state. Figures 8(c) and (d) show the TNE behaviors from the perspective of $\Delta_{3,1,\alpha}^{B*}$. Compared to $\overline{\Delta_{3,1,x}^{B*}}$, the $\overline{\Delta_{3,1,y}^{B*}}$ exhibits more significant amplitude. The $\overline{\Delta_{3,1,x}^{B*}}$ is symmetric about the line $y = 0.6$ and $\overline{\Delta_{3,1,y}^{B*}}$ is symmetric about the origin point. The Pr number has limited effects on $\overline{\Delta_{3,1,x}^{B*}}$ and $\overline{\Delta_{3,1,y}^{B*}}$ since it does not directly change the heat conductivity coefficient in the ES-BGK model. There are two points that should be stated: (i) It is essential to note that the above descriptions are based on the results at a typical moment $t = 0.02$. Descriptions of other moments are equally important for a comprehensive understanding of the kinetic behaviors during the SBI process. (ii) Moreover, higher-order TNE quantities ($\Delta_{3,\alpha\beta\gamma}^{B*}$ and $\Delta_{4,2,\alpha\beta}^{B*}$) contain more condensed information and are also closely related to the gradients of macroscopic quantities.

To qualitatively investigate the viscous effects on the temporal evolution of TNE features, Fig. 9(a) plots the temporal profiles of $d^{\sigma*}$. This quantity can be used to describe roughly the total TNE strength of the whole fluid field. It can be seen that the peaks (valleys) of d^A* and d^B* profiles are closely related to the location of the shock wave. Here t_1 indicates the moment that the incident shock has just passed the bubble and t_2 represents the moment when the incident shock runs out of the fluid field. It is shown that the viscosity simultaneously raises the TNE strength of both components A and B . Fig. 9(b) displats the total TNE strength of the fluid field from two rel-

atively microscopic perspectives. The temporal evolution of $d_2^{\sigma*}$ and $d_{3,1}^{\sigma*}$ are both analyzed in the figure. Lines with different colors indicate cases with different TNE components, and different symbols represent different viscosities. For component B (the bubble), the viscosity enhances significantly the strength of d_2^B* but hardly changed the strength of $d_{3,1}^B*$. The reason is that when adjusting the Pr number, it does not modify directly the heat conductivity coefficient. For component A (the ambient gas), the situation is reversed, i.e., the viscosity enhances significantly the strength of $d_{3,1}^A*$ but almost maintains the strength of d_2^A* . The reason is attributed to the fact that a fluid with higher viscosity exhibits enhanced capacity for absorbing energy from shock waves, thereby resulting in an elevated heat flux.

The entropy production rate and entropy production, which are significant in the compression science field, are also analyzed. There are two kinds of entropy production rates⁵⁰:

$$\dot{S}_{\text{NOEF}} = \int \Delta_{3,1}^* \cdot \nabla \frac{1}{T} dr, \quad (19)$$

$$\dot{S}_{\text{NOMF}} = \int -\frac{1}{T} \Delta_2^* : \nabla u dr. \quad (20)$$

The former is caused by the NOEF and the temperature gradient, and the latter is contributed by the NOMF and the velocity gradient. Fig. 10(a) plots the temporal evolution of entropy production rates \dot{S}_{NOEF} and \dot{S}_{NOMF} . It can be seen that the changes of curves of the entropy generation rate are closely related to the position of the shock wave. For \dot{S}_{NOMF} , their values increase continuously during the incident shock

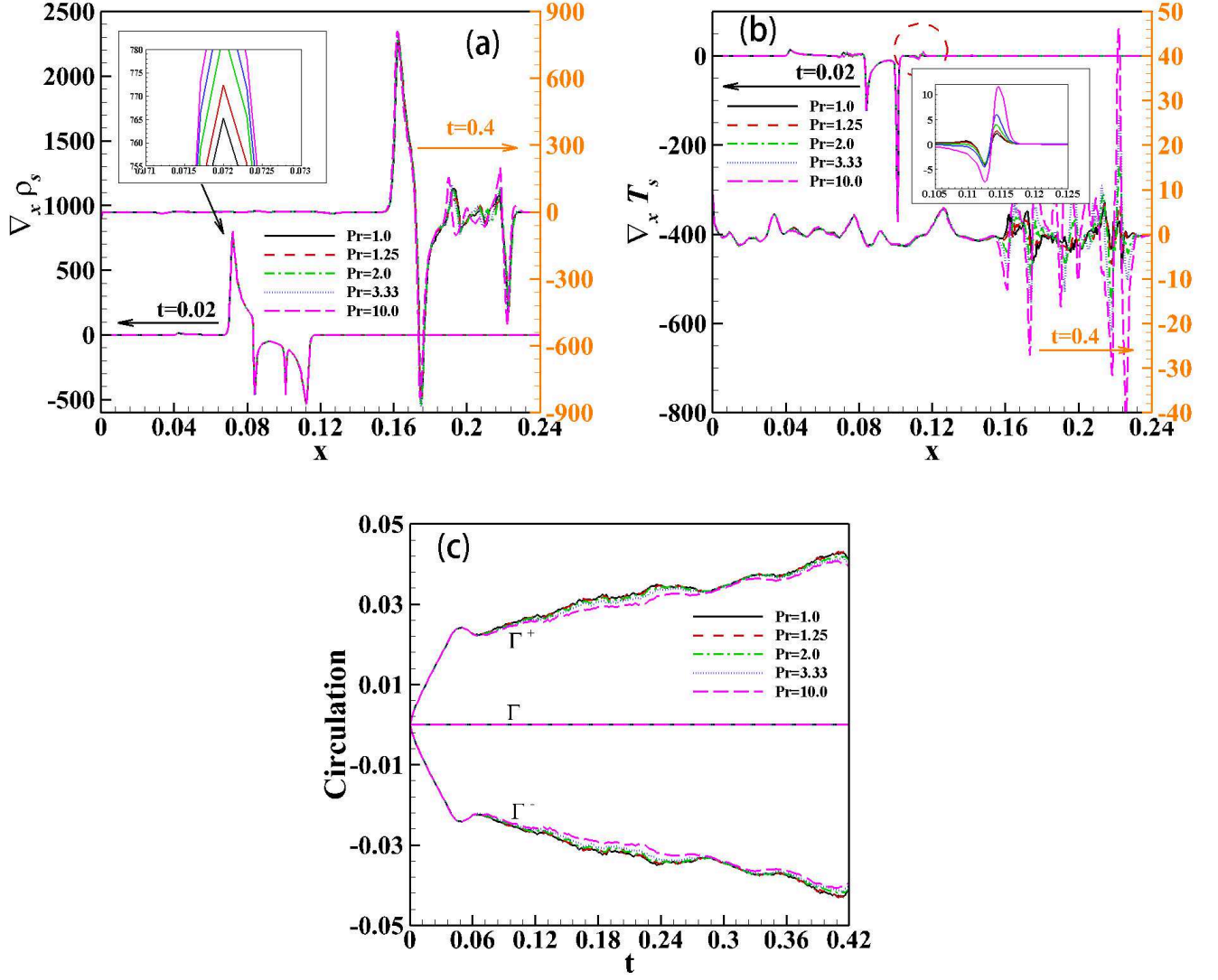


FIG. 5. (a) The profiles of $\nabla_x \rho_s$ at $t = 0.02$ and $t = 0.4$, respectively. (b) The profiles of $\nabla_x T_s$ at $t = 0.02$ and $t = 0.4$, respectively. (c) Temporal evolution of circulation of the bubble during the SBI process.

wave acts on the bubble ($t < t_1$). Later, the values of \dot{S}_{NOMF} decrease. When the incident shock wave runs out of the fluid field ($t > t_2$), the \dot{S}_{NOMF} reduce rapidly and subsequently maintain their values for a longer time. For \dot{S}_{NOEF} , before t_2 , their values reduce and then increase. When $t > t_2$, they show an upward trend. Theoretically, viscosity affects the TNE quantities through influencing the transport coefficient and gradients of macroscopic quantity. The viscosity raises significantly the \dot{S}_{NOMF} through increasing the transport coefficient, and amplifies the \dot{S}_{NOEF} by increasing the temperature gradient. Summing the entropy generation rate over this period, the entropy generations (S_{NOEF} and S_{NOMF}) during this period can be obtained. Fig. 10(b) shows the entropy generations of cases with different viscosities. It can be seen that both the two types of entropy generation increase as the viscosity increases. Before $Pr < Pr_c$, the S_{NOMF} is larger than S_{NOEF} . When $Pr > Pr_c$, the situation is reversed.

IV. Conclusions

A two-fluid DBM with a flexible Pr number is designed to investigate the influence of viscosity on the morphological and TNE characterizations during the SBI process. Different from most of the previous research that relied on traditional macroscopic models/methods, this paper studies the dynamic and kinetic processes of SBI from a mesoscopic view. Morphologically, the viscosity affects the shape of the vortex pair, increases both the gradients of density and temperature of the fluid field, reduces the values of the circulation of the bubble, and inhibits the bubble's shear motion. To provide a more comprehensive description of the SBI process, two Minkowski measures are introduced: the proportion A of the area occupied by the high-density region and the boundary length L separating the high- and low-density regions. The viscosity increases both the proportion A and boundary length

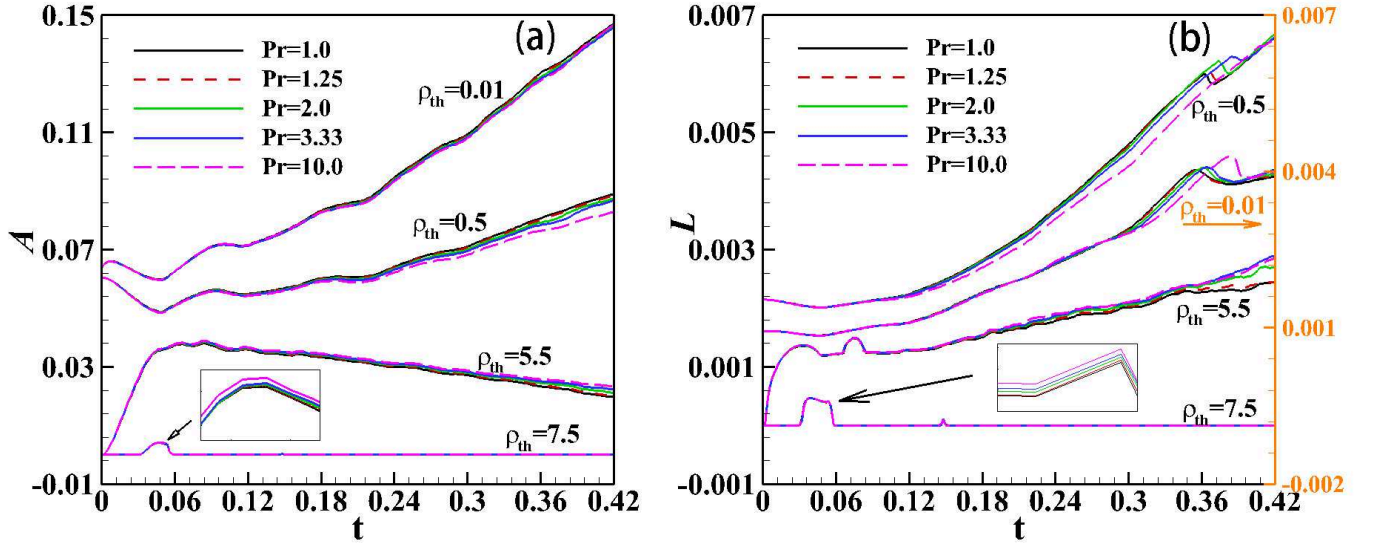


FIG. 6. (a) The temporal evolution of proportion A . (b) The temporal evolution of boundary length L . Four cases with different density threshold values are plotted.

L when selecting the threshold as $\rho_{th} > \rho_0$, but it reduces them when $\rho_{th} < \rho_0$, where ρ_0 is the initial density of the bubble. The underlying reason is that the fluid with a higher viscosity exhibits enhanced capacity for absorbing energy from shock waves, making it easier to increase the density during the compression process.

The spatiotemporal features of TNE quantities are analyzed from multiple perspectives. These results from multiple perspective together constitute a relatively complete depiction of the SBI. Contours of $|\Delta_2^{\sigma*}|$ and $|\Delta_{3,1}^{\sigma*}|$ demonstrate significant deviations from thermodynamic equilibrium at the contact interfaces with macroscopic quantity gradients. However, the regions far from the interface remain close to the equilibrium state. The spatial configuration of $\Delta_{2,\alpha\beta}^{\sigma*}$ and $\Delta_{3,1,\alpha}^{\sigma*}$ exhibit interesting symmetry. Theoretically, viscosity influences these TNE quantities through affecting the transport coefficient and gradients of macroscopic quantity. When increasing the viscosity of component B , until the shock wave interacts with the bubble, the viscosity enhances significantly the strength of $\Delta_{2,\alpha\beta}^{B*}$ by directly amplifying the transport coefficient directly. However, at this moment, the influence of gradients of macroscopic quantity is not significant, leading to almost no effect on the strengths of $\Delta_{2,\alpha\beta}^{A*}$ and $\Delta_{3,1,\alpha}^{\sigma*}$. The viscosity increases the total TNE strengths $d^{\sigma*}$, d_2^{B*} , and $d_{3,1}^{A*}$, but has little influence on the strength of d_2^{A*} and $d_{3,1}^{B*}$. Through raising the transport coefficient and the temperature gradient, respectively, the viscosity increases the two types of entropy production rates and their corresponding entropy production. The fundamental research in this paper enhances our understanding of the SBI mechanism in various applications, such as inertial confinement fusion, supersonic combustors, underwater explosions, etc.

Acknowledgments

The authors thank Chuandong Lin, Feng Chen, Ge Zhang, Yiming Shan, Jie Chen and Hanwei Li on helpful discussions for DBM. This work was supported by the National Natural Science Foundation of China (Nos. 12172061, 11875001, and 12102397), the Strategic Priority Research Program of Chinese Academy of Sciences (No. XDA25051000), the opening project of State Key Laboratory of Explosion Science and Technology (Beijing Institute of Technology) (No. KFJJ23-02M), Foundation of National Key Laboratory of Computational Physics, Foundation of National Key Laboratory of Shock Wave and Detonation Physics, and Hebei Natural Science Foundation (No. A2021409001), Central Guidance on Local Science and Technology Development Fund of Hebei Province (No. 226Z7601G), and “Three, Three and Three Talent Project” of Hebei Province (No. A202105005).

A. Expressions of the kinetic moments of $f^{\sigma,ES}$

The kinetic moments can be obtained by integrating the Eq. (3) in the particle velocity space \mathbf{v} . Their expressions are as follows:

$$M_0^{\sigma,ES} = \sum_i f_i^{\sigma,ES} = \rho^\sigma, \quad (A1)$$

$$M_{1,x}^{\sigma,ES} = \sum_i f_i^{\sigma,ES} v_{ix} = \rho^\sigma u_x, \quad (A2)$$

$$M_{1,y}^{\sigma,ES} = \sum_i f_i^{\sigma,ES} v_{iy} = \rho^\sigma u_y, \quad (A3)$$

$$M_{2,xy}^{\sigma,ES} = \sum_i f_i^{\sigma,ES} v_{ix} v_{iy} = \rho^\sigma (\lambda_{xy} + u_x u_y), \quad (A4)$$

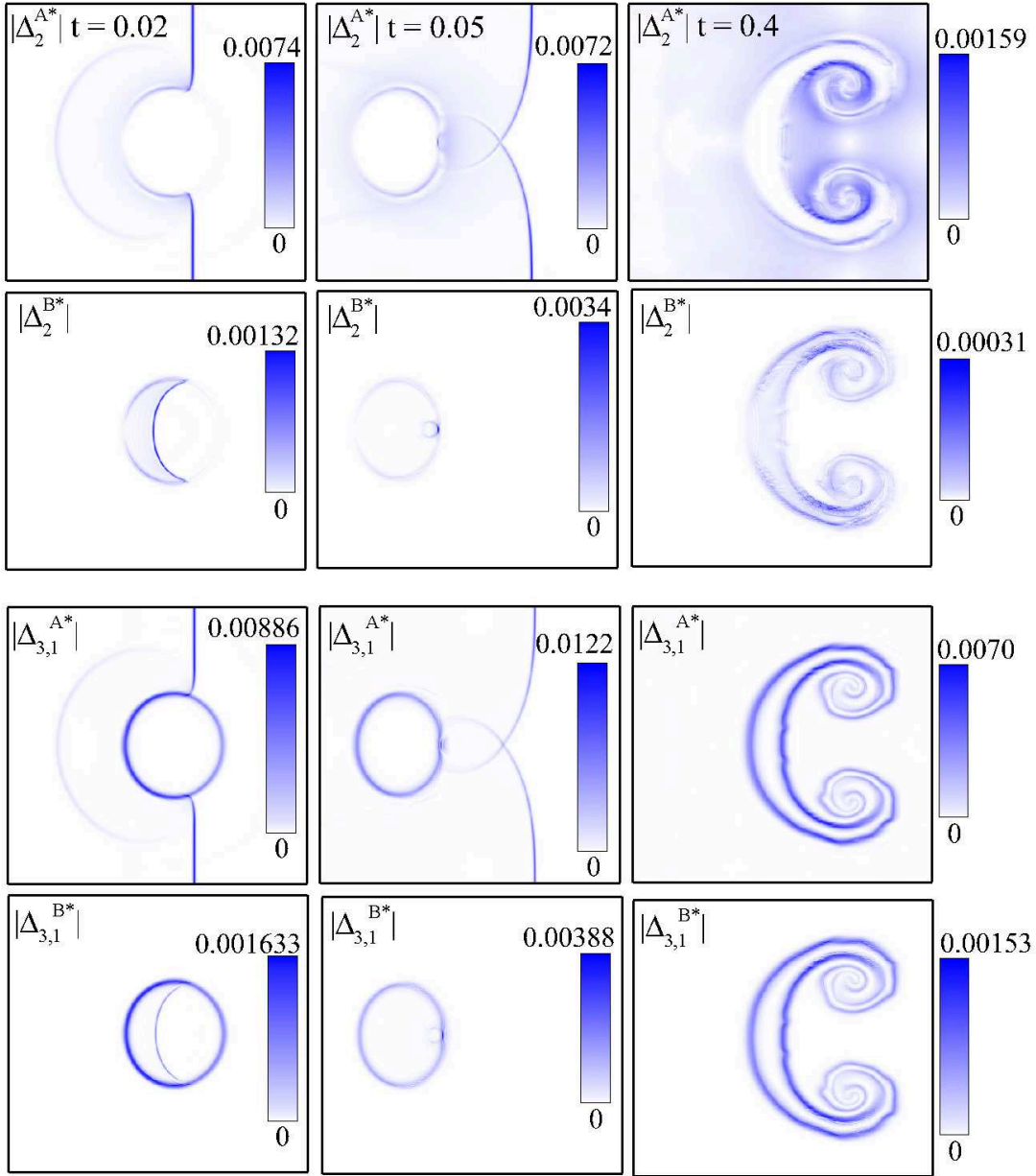


FIG. 7. Contours of $|\Delta_2^{\sigma,*}|$ and $|\Delta_{3,1}^{\sigma,*}|$ at three different moments.

$$M_{2,xx}^{\sigma,ES} = \sum_i f_i^{\sigma,ES} v_{ix}^2 = \rho^\sigma (\lambda_{xx} + u_x^2), \quad (\text{A5})$$

$$M_{3,yyy}^{\sigma,ES} = \sum_i f_i^{\sigma,ES} v_{iy}^3 = \rho^\sigma u_y (3\lambda_{yy} + u_y^2), \quad (\text{A10})$$

$$M_{2,yy}^{\sigma,ES} = \sum_i f_i^{\sigma,ES} v_{iy}^2 = \rho^\sigma (\lambda_{yy} + u_y^2), \quad (\text{A6})$$

$$M_{3,xxx}^{\sigma,ES} = \sum_i f_i^{\sigma,ES} v_{ix}^3 = \rho^\sigma u_x (3\lambda_{xx} + u_x^2), \quad (\text{A7})$$

$$M_{4,2,xx}^{\sigma,ES} = \sum_i f_i^{\sigma,ES} \frac{1}{2} v_{ix}^2 v_{i\alpha}^2 = \frac{1}{2} \rho^\sigma [\lambda_{xx} (\lambda_{yy} + 6u_x^2 + u_y^2) + 3\lambda_{xx}^2 + 4\lambda_{xy} u_x u_y + 2\lambda_{xy}^2 + u_x^2 (\lambda_{yy} + u_x^2 + u_y^2)], \quad (\text{A11})$$

$$M_{3,xy}^{\sigma,ES} = \sum_i f_i^{\sigma,ES} v_{ix}^2 v_{iy} = \rho^\sigma [2\lambda_{xy} u_x + u_y (\lambda_{xx} + u_x^2)], \quad (\text{A8})$$

$$M_{3,xyy}^{\sigma,ES} = \sum_i f_i^{\sigma,ES} v_{ix} v_{iy}^2 = \rho^\sigma u_x [2\lambda_{xy} u_y + u_x (\lambda_{yy} + u_y^2)], \quad (\text{A9})$$

$$M_{4,2,xy}^{\sigma,ES} = \sum_i f_i^{\sigma,ES} \frac{1}{2} v_{ix} v_{iy} v_{i\alpha}^2 = \frac{1}{2} \rho^\sigma [3\lambda_{xx} (\lambda_{xy} + u_x u_y) + 3\lambda_{xy} (\lambda_{yy} + u_x^2 + u_y^2) + u_x u_y (3\lambda_{yy} + u_x^2 + u_y^2)], \quad (\text{A12})$$

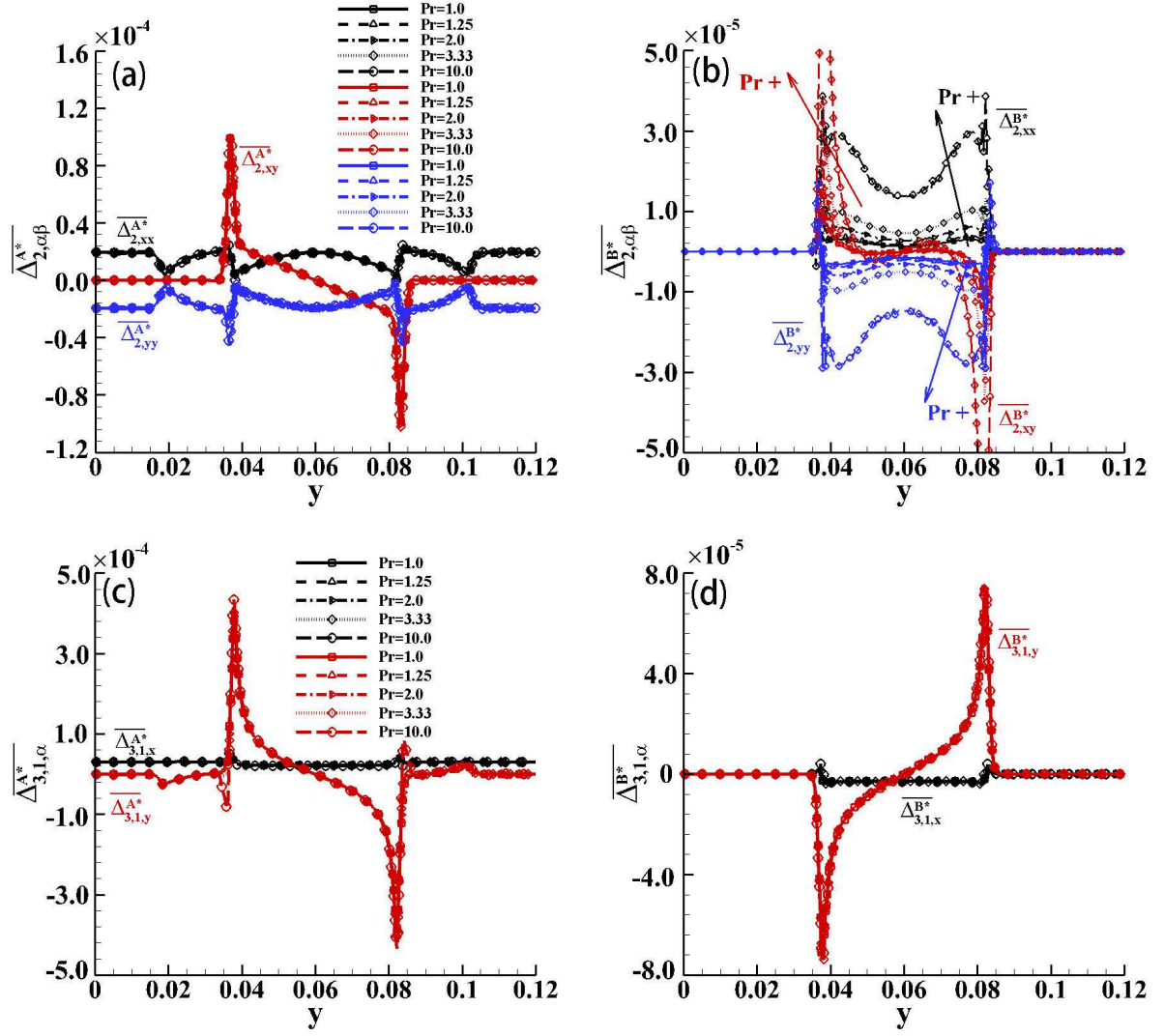


FIG. 8. (a) The profiles of $\overline{\Delta_{2,\alpha\beta}^{A*}}$. (b) The profiles of $\overline{\Delta_{2,\alpha\beta}^{B*}}$. (c) The profiles of $\overline{\Delta_{3,1,\alpha}^{A*}}$. (d) The profiles of $\overline{\Delta_{3,1,\alpha}^{B*}}$.

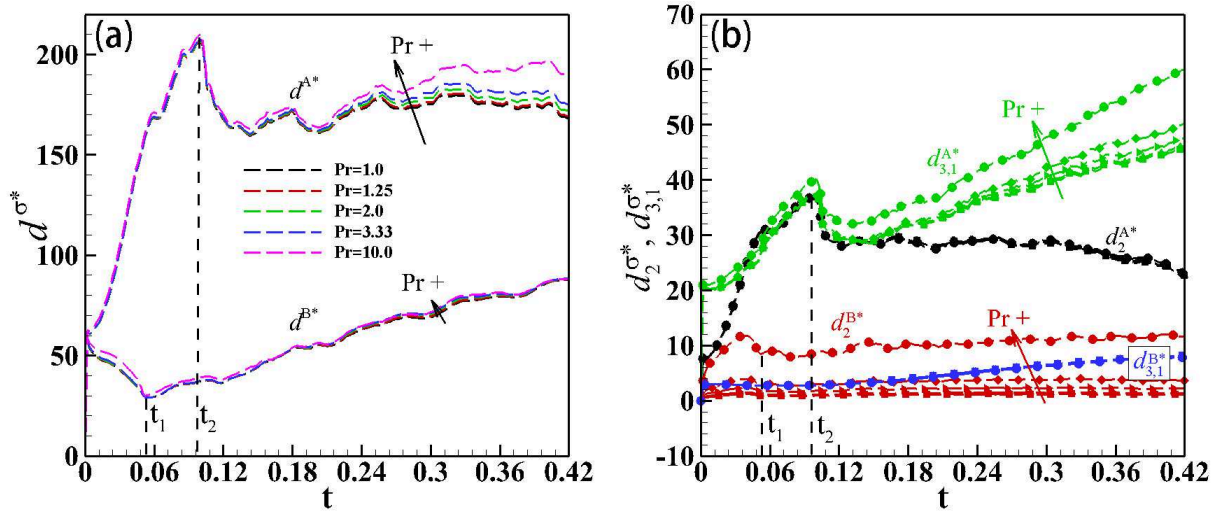


FIG. 9. (a) The temporal evolution of d^{A*} and d^{B*} . (b) The temporal evolution of $d_2^{\sigma*}$ and $d_{3,1}^{\sigma*}$.

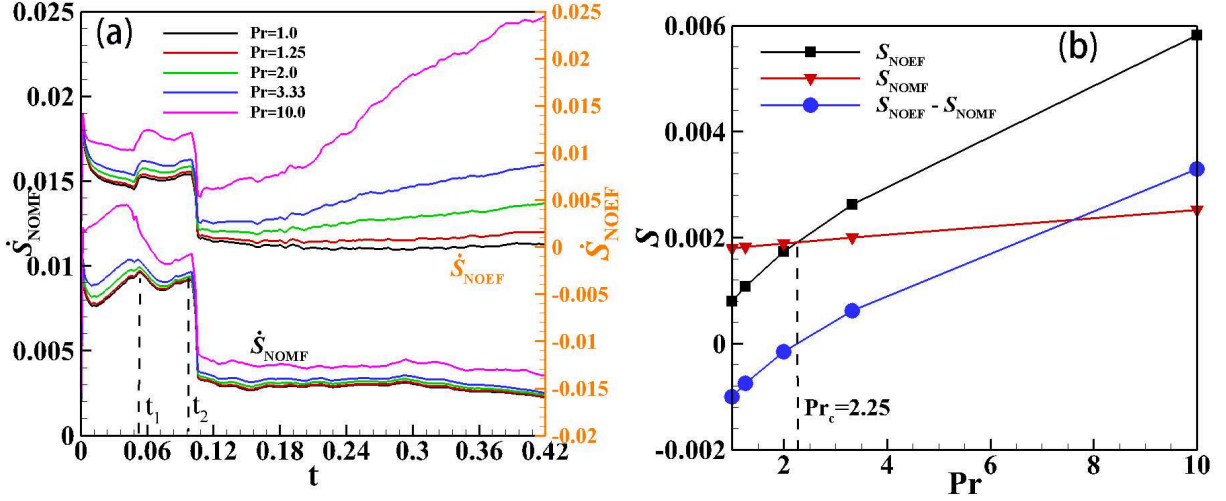


FIG. 10. (a) The temporal evolution of entropy production rates \dot{S}_{NOEF} and \dot{S}_{NOMF} . (b) Entropy productions (S_{NOEF} , S_{NOMF} , and $S_{\text{NOEF}} - S_{\text{NOMF}}$) over this period.

$$M_{4,2,yy}^{\sigma,ES} = \sum_i f_i^{\sigma,ES} \frac{1}{2} v_{iy}^2 v_{ia}^2 = \frac{1}{2} \rho^\sigma [u_y^2 (\lambda_{xx} + 6\lambda_{yy} + u_x^2) + \lambda_{yy} (\lambda_{xx} + 3\lambda_{yy} + u_x^2) + 4\lambda_{xy} u_x u_y + 2\lambda_{xy}^2 + u_y^4], \quad (\text{A13})$$

The modified term $\lambda_{\alpha\beta} = R^\sigma T \delta_{\alpha\beta} + \frac{b^\sigma}{\rho^\sigma} \Delta_{2,\alpha\beta}^{\sigma*}$ with $\Delta_{2,\alpha\beta}^{\sigma*} = \sum_i (f_i^\sigma - f_i^{\sigma,eq}) \mathbf{v}_i^* \mathbf{v}_i^*$. The two contracted moments can be expressed by the corresponding non-contracted moments, i.e.,

$$M_{2,0}^{\sigma,ES} = \frac{1}{2} (M_{2,xx}^{\sigma,ES} + M_{2,yy}^{\sigma,ES}) \quad (\text{A14})$$

$$M_{3,1,x}^{\sigma,ES} = \frac{1}{2} (M_{3,xxx}^{\sigma,ES} + M_{3,xyy}^{\sigma,ES}) \quad (\text{A15})$$

$$M_{3,1,y}^{\sigma,ES} = \frac{1}{2} (M_{3,yyy}^{\sigma,ES} + M_{3,xyx}^{\sigma,ES}) \quad (\text{A16})$$

When $b^\sigma = 0$, the ES-BGK model is simplified to BGK model. So the kinetic moments of $f^{\sigma,eq}$ can be obtained easily by submitting $b^\sigma = 0$ into the kinetic moments of $f^{\sigma,ES}$.

B. Two-fluid hydrodynamic equations

In this part, the expressions of hydrodynamic equations derived from the ES-BGK Boltzmann equation through the CE multiscale analysis are given. More detailed derivations can see the reference presented by Zhang *et al.*⁵⁶. The NS equations for component σ are:

$$\frac{\partial \rho^\sigma}{\partial t} + \frac{\partial}{\partial r_\alpha} (\rho^\sigma u_\alpha^\sigma) = 0, \quad (\text{B1})$$

$$\begin{aligned} \frac{\partial}{\partial t} (\rho^\sigma u_\alpha^\sigma) + \frac{\partial (p^\sigma \delta_{\alpha\beta} + \rho^\sigma u_\alpha^\sigma u_\beta^\sigma)}{\partial r_\beta} + \frac{\partial (P_{\alpha\beta}^\sigma + U_{\alpha\beta}^\sigma)}{\partial r_\beta} \\ = -\frac{\rho^\sigma}{\tau^\sigma} (u_\alpha^\sigma - u_\alpha), \end{aligned} \quad (\text{B2})$$

$$\begin{aligned} \frac{\partial}{\partial t} (\rho^\sigma E_T^\sigma) + \frac{\partial}{\partial r_\alpha} (\rho^\sigma E_T^\sigma + p^\sigma) u_\alpha^\sigma + \frac{\partial}{\partial r_\beta} [u_\beta^\sigma (P_{\alpha\beta}^\sigma + U_{\alpha\beta}^\sigma) \\ - \kappa^\sigma \frac{\partial T^\sigma}{\partial r_\alpha} + Y_\alpha^\sigma] = -\frac{\rho^\sigma}{\tau^\sigma} \left[\frac{D(T^\sigma - T)}{2} + \frac{1}{2} (u_\alpha^{\sigma 2} - u_\alpha^2) \right]. \end{aligned} \quad (\text{B3})$$

where

$$E_T^\sigma = \frac{1}{2} (DT^\sigma + u_\alpha^{\sigma 2}), \quad (\text{B4})$$

$$P_{\alpha\beta}^\sigma = -\mu^\sigma \left(\frac{\partial u_\alpha^\sigma}{\partial r_\beta} + \frac{\partial u_\beta^\sigma}{\partial r_\alpha} - \frac{2}{D} \frac{\partial u_\gamma^\sigma}{\partial r_\gamma} \delta_{\alpha\beta} \right), \quad (\text{B5})$$

$$U_{\alpha\beta}^\sigma = \rho^\sigma [(u_\beta - u_\beta^\sigma)(u_\alpha - u_\alpha^\sigma) + \frac{1}{D} (u_\alpha^\sigma - u_\alpha)^2 \delta_{\alpha\beta}], \quad (\text{B6})$$

$$\begin{aligned} Y_\alpha^\sigma = \left[\frac{D+2}{2} \rho^\sigma R^\sigma (T^\sigma - T) (u_\alpha^\sigma - u_\alpha) - \frac{D+4}{2D} \rho^\sigma (u_\alpha^\sigma - u_\alpha)^2 u_\alpha^\sigma \right. \\ \left. + \rho^\sigma u_\alpha^\sigma (u_\alpha^\sigma - u_\alpha) u_\alpha^\sigma - \rho^\sigma u_\beta^\sigma (u_\alpha u_\beta - u_\alpha u_\beta^\sigma) \right] \\ + \frac{1}{2} \rho^\sigma (u_\alpha^2 - u_\alpha^{\sigma 2}) u_\alpha. \end{aligned} \quad (\text{B7})$$

Performing \sum_σ on both sides of the three equations gives the NS hydrodynamic equations describing the whole system, i.e.,

$$\frac{\partial \rho}{\partial t} + \frac{\partial}{\partial r_\alpha} (\rho u_\alpha) = 0, \quad (\text{B8})$$

$$\begin{aligned} \frac{\partial}{\partial t} (\rho u_\alpha) + \frac{\frac{\partial \sum_\sigma (p^\sigma \delta_{\alpha\beta} + \rho^\sigma u_\alpha^\sigma u_\beta^\sigma)}{\partial r_\beta}}{\partial r_\beta} \\ + \frac{\frac{\partial \sum_\sigma (P_{\alpha\beta}^\sigma + U_{\alpha\beta}^\sigma)}{\partial r_\beta}}{\partial r_\beta} = 0, \end{aligned} \quad (\text{B9})$$

$$\begin{aligned} & \frac{\partial}{\partial t}(\rho E_T) + \frac{\partial}{\partial r_\alpha} \sum_\sigma (\rho^\sigma E_T^\sigma + p^\sigma) u_\alpha^\sigma \\ & + \frac{\partial}{\partial r_\beta} \sum_\sigma [u_\beta^\sigma (P_{\alpha\beta}^\sigma + U_{\alpha\beta}^\sigma) - \kappa^\sigma \frac{\partial T^\sigma}{\partial r_\alpha} + Y_\alpha^\sigma] = 0. \end{aligned} \quad (\text{B10})$$

The dynamic viscosity efficient is $\mu^\sigma = \text{Pr}^\sigma \tau^\sigma p^\sigma = \frac{1}{1-\text{Pr}^\sigma} \tau^\sigma p^\sigma$, with $p^\sigma = \rho^\sigma R^\sigma T^\sigma$. The heat conductivity is $\kappa^\sigma = C_p^\sigma \tau^\sigma p^\sigma$, with $C_p^\sigma = \frac{D+2}{2} R^\sigma$. It should be pointed out again that recovering the hydrodynamic equations is only one part of the physical function of DBM. The physical function of DBM corresponds to the EHEs. Deriving the hydrodynamic equations is used to verify the correctness of physical modeling. In DBM, it does not need to solve the hydrodynamic equations in DBM simulation.

Data Availability

The data that support the findings of this study are available from the corresponding author upon reasonable request.

References

- ¹D. Ranjan, J. Oakley, and R. Bonazza, “Shock-bubble interactions,” *Annu. Rev. Fluid Mech.* **43**, 117–140 (2011).
- ²D. Ranjan, J. Niederhaus, B. Motl, M. Anderson, J. Oakley, and R. Bonazza, “Experimental investigation of primary and secondary features in high-Mach-number shock-bubble interaction,” *Phys. Rev. Lett.* **98**, 024502 (2007).
- ³H. Liu, B. Yu, B. Zhang, and Y. Xiang, “On mixing enhancement by secondary baroclinic vorticity in a shock–bubble interaction,” *J. Fluid Mech.* **931** (2022).
- ⁴B. Yu, H. Liu, and H. Liu, “Scaling behavior of density gradient accelerated mixing rate in shock bubble interaction,” *Phys. Rev. Fluids* **6**, 064502 (2021).
- ⁵L. Zou, S. Liao, C. Liu, Y. Wang, and Z. Zhai, “Aspect ratio effect on shock-accelerated elliptic gas cylinders,” *Phys. Fluids* **28**, 036101 (2016).
- ⁶E. Fan, J. Hao, B. Guan, C.-y. Wen, and L. Shi, “Numerical investigation on reacting shock-bubble interaction at a low Mach limit,” *Combust. Flame* **241**, 112085 (2022).
- ⁷Y. Liang, Z. Zhai, and X. Luo, “Interaction of strong converging shock wave with SF₆ gas bubble,” *Sci. China Phys. Mech.* **61**, 1–9 (2018).
- ⁸U. Hwang, K. A. Flanagan, and R. Petre, “Chandra X-ray observation of a Mature Cloud-Shock Interaction in the Bright Eastern Knot Region of Puppis A,” *Astrophysical J.* **635**, 355–364 (2005).
- ⁹F. Diegelmann, S. Hickel, and N. A. Adams, “Three-dimensional reacting shock–bubble interaction,” *Combust. Flame* **181**, 300–314 (2017).
- ¹⁰Y. X. Liu, Z. Chen, L. F. Wang, Z. Y. Li, J. F. Wu, W. H. Ye, and Y. J. Li, “Dynamic of shock–bubble interactions and nonlinear evolution of ablative hydrodynamic instabilities initiated by capsule interior isolated defects,” *Phys. Plasmas* **30** (2023).
- ¹¹R. Samtaney and N. J. Zabusky, “Circulation deposition on shock-accelerated planar and curved density-stratified interfaces: models and scaling laws,” *J. Fluid Mech.* **269**, 45–78 (1994).
- ¹²J. Yang, T. Kubota, and E. E. Zukoski, “A model for characterization of a vortex pair formed by shock passage over a light-gas inhomogeneity,” *J. Fluid Mech.* **258**, 217–244 (1994).
- ¹³G. Layes, G. Jourdan, and L. Houas, “Distortion of a spherical gaseous interface accelerated by a plane shock wave,” *Phys. Rev. Lett.* **91**, 174502 (2003).
- ¹⁴J.-F. Haas and B. Sturtevant, “Interaction of weak shock waves with cylindrical and spherical gas inhomogeneities,” *J. Fluid Mech.* **181**, 41–76 (1987).
- ¹⁵Z. Zhai, J. Ou, and J. Ding, “Coupling effect on shocked double-gas cylinder evolution,” *Phys. Fluids* **31**, 096104 (2019).
- ¹⁶J. Picone and J. Boris, “Vorticity generation by shock propagation through bubbles in a gas,” *J. Fluid Mech.* **189**, 23–51 (1988).
- ¹⁷L. Zou, Z. Zhai, J. Liu, Y. Wang, and C. Liu, “Energy convergence effect and jet phenomenon of shock-heavy spherical bubble interaction,” *Sci. China Physics. Mech.* **58**, 1–7 (2015).
- ¹⁸S. Sha, Z. Chen, and Q. Zhang, “Numerical investigations on the interaction of shock waves with spherical SF₆ bubbles (in chinese),” *Acta Physica Sinica*, **64**, 015201 (2015).
- ¹⁹Y. Zhu, L. Yu, J. Pan, Z. Pan, and P. Zhang, “Jet formation of SF₆ bubble induced by incident and reflected shock waves,” *Phys. Fluids* **29**, 126105 (2017).
- ²⁰D. Li, G. Wang, and B. Guan, “On the circulation prediction of shock-accelerated elliptical heavy gas cylinders,” *Phys. Fluids* **31**, 056104 (2019).
- ²¹J. Chen, F. Qu, X. Wu, Z. Wang, and J. Bai, “Numerical study of interactions between shock waves and a circular or elliptic bubble in air medium,” *Phys. Fluids* **33**, 043301 (2021).
- ²²J. Ding, T. Si, M. Chen, Z. Zhai, X. Lu, and X. Luo, “On the interaction of a planar shock with a three-dimensional light gas cylinder,” *J. Fluid Mech.* **828**, 289–317 (2017).
- ²³J. Ding, Y. Liang, M. Chen, Z. Zhai, T. Si, and X. Luo, “Interaction of planar shock wave with three-dimensional heavy cylindrical bubble,” *Phys. Fluids* **30**, 106109 (2018).
- ²⁴T. Si, Z. Zhai, and X. Luo, “Experimental study of Richtmyer-Meshkov instability in a cylindrical converging shock tube,” *Laser and Particle Beams* **32**, 343–351 (2014).
- ²⁵T. Si, Z. Zhai, J. Yang, and X. Luo, “Experimental investigation of reshocked spherical gas interfaces,” *Phys. Fluids* **24**, 054101 (2012).
- ²⁶Z. Zhai, F. Zhang, T. Si, and X. Luo, “Evolution of heavy gas cylinder under reshock conditions,” *J. Visualization* **17**, 123–129 (2014).
- ²⁷D. Zhang, A. Xu, Y. Zhang, Y. Gan, and Y. Li, “Discrete Boltzmann modeling of high-speed compressible flows with various depths of non-equilibrium,” *Phys. Fluids* **34**, 086104 (2022).
- ²⁸B. Zhang, H. Chen, B. Yu, M. He, and H. Liu, “Molecular simulation on viscous effects for microscale combustion in reactive shock-bubble interaction,” *Combust. Flame* **208**, 351–363 (2019).
- ²⁹Y. Gan, A. Xu, G. Zhang, Y. Li, and H. Li, “Phase separation in thermal systems: A lattice Boltzmann study and morphological characterization,” *Phys. Rev. E* **84**, 046715 (2011).
- ³⁰H. Lai, A. Xu, G. Zhang, Y. Gan, Y. Ying, and S. Succi, “Nonequilibrium thermohydrodynamic effects on the Rayleigh-Taylor instability in compressible flows,” *Phys. Rev. E* **94**, 023106 (2016).
- ³¹C. Lin, A. Xu, G. Zhang, K. Luo, and Y. Li, “Discrete Boltzmann modeling of Rayleigh-Taylor instability in two-component compressible flows,” *Phys. Rev. E* **96**, 053305 (2017).
- ³²C. Lin, K. Luo, A. Xu, Y. Gan, and H. Lai, “Multiple-relaxation-time discrete Boltzmann modeling of multicomponent mixture with nonequilibrium effects,” *Phys. Rev. E* **103**, 013305 (2021).
- ³³F. Chen, A. Xu, and G. Zhang, “Collaboration and Competition Between Richtmyer-Meshkov instability and Rayleigh-Taylor instability,” *Phys. Fluids* **30**, 102105 (2018).
- ³⁴Y. Gan, A. Xu, G. Zhang, C. Lin, H. Lai, and Z. Liu, “Nonequilibrium and morphological characterizations of Kelvin-Helmholtz instability in compressible flows,” *Front. Phys.* **14**, 43602 (2019).
- ³⁵J. Chen, A. Xu, D. Chen, Y. Zhang, and Z. Chen, “Discrete Boltzmann modeling of Rayleigh-Taylor instability: effects of interfacial tension, viscosity and heat conductivity,” *Phys. Rev. E* **106**, 015102 (2022).
- ³⁶H. Li, A. Xu, G. Zhang, and Y. Shan, “Rayleigh-Taylor instability under multi-mode perturbation: Discrete Boltzmann modeling with tracers,” *Commun. Theor. Phys.* **74**, 115601 (2022).
- ³⁷Y. Shan, A. Xu, Y. Zhang, L. Wang, and F. Chen, “Discrete Boltzmann modeling of detonation: Based on the Shakhov model,” *J. Mech. Eng. Sci.* **237**, 2517–2531 (2022).
- ³⁸Z. Liu, J. Song, A. Xu, Y. Zhang, and K. Xie, “Discrete Boltzmann modeling of plasma shock wave,” *J. Mech. Eng. Sci.* **237**, 2532–2548 (2022).
- ³⁹G. Zhang, A. Xu, D. Zhang, Y. Li, H. Lai, and X. Hu, “Delineation of the flow and mixing induced by Rayleigh-Taylor instability through tracers,” *Phys. Fluids* **33**, 076105 (2021).

- ⁴⁰F. Chen, A. Xu, Y. Zhang, Y. Gan, B. Liu, and S. Wang, “Effects of the initial perturbations on the Rayleigh-Taylor-Kelvin-Helmholtz instability system,” *Front. Phys.* **17**, 33505 (2022).
- ⁴¹D. Zhang, A. Xu, J. S. Y. Gan, Y. Zhang, and Y. Li, “Specific-heat ratio effects on the interaction between shock wave and heavy-cylindrical bubble: Based on discrete boltzmann method,” *Compu. & Fluids*.
- ⁴²L. Chen, H. Lai, C. Lin, and D. Li, “Specific heat ratio effects of compressible Rayleigh-Taylor instability studied by discrete Boltzmann method,” *Front. Phys.* **16**, 52500 (2021).
- ⁴³X. Su and C. Lin, “Nonequilibrium effects of reactive flow based on gas kinetic theory,” *Commun. Theor. Phys.* **74**, 035604 (2022).
- ⁴⁴S. Singh, M. Battiatto, and R. Myong, “Impact of bulk viscosity on flow morphology of shock-accelerated cylindrical light bubble in diatomic and polyatomic gases,” *Phys. Fluids* **33**, 066103 (2021).
- ⁴⁵The DBM can be interpreted as discrete Boltzmann method/model/modeling according the specific context.
- ⁴⁶A. Xu and Y. Zhang, “Complex media kinetics (in chinese),” (Beijing: Science Press, 2022).
- ⁴⁷Y. Gan, A. Xu, H. Lai, W. Li, G. Sun, and S. Succi, “Discrete boltzmann multi-scale modelling of non-equilibrium multiphase flows,” *J. Fluid Mech.* **951**, A8 (2022).
- ⁴⁸Y. Zhang, A. Xu, F. Chen, C. Lin, and Z. Wei, “Non-equilibrium characteristics of mass and heat transfers in the slip flow,” *AIP Adv.* **12**, 035347 (2022).
- ⁴⁹Y. Zhang, A. Xu, G. Zhang, Z. Chen, and P. Wang, “Discrete ellipsoidal statistical BGK model and Burnett equations,” *Front. Phys.* **13**, 135101 (2017).
- ⁵⁰Y. Zhang, A. Xu, G. Zhang, Y. Gan, Z. Chen, and S. Succi, “Entropy production in thermal phase separation: a kinetic-theory approach,” *Soft Matter* **15**, 2245–2259 (2019).
- ⁵¹A. Xu, Y. Shan, F. Chen, Y. Gan, and C. Lin, “Progress of mesoscale modeling and investigation of combustion multiphase flow (in chinese),” *Acta Aeronautica et Astronautica Sinica* **42**, 625842 (2021).
- ⁵²A. Xu, J. Song, F. Chen, K. Xie, and Y. Ying, “Modeling and Analysis Methods for Complex Fields Based on Phase Space (in chinese),” *Chinese Journal of Computational Physics* **38**, 631–660 (2021).
- ⁵³A. Xu, J. Chen, J. Song, D. Chen, and Z. Chen, “Progress of discrete boltzmann study on multiphase complex flows (in chinese),” *Acta Aerodynamica Sinica* **39**, 138–169 (2021).
- ⁵⁴A. G. Xu, G. C. Zhang, X. F. Pan, P. Zhang, and J. S. Zhu, “Morphological characterization of shocked porous material,” *J. Phys. D Appl. Phys.* **42**, 075409 (2009).
- ⁵⁵J. Lowell H. Holway, “New statistical models for kenitic theory: methods of construction,” *Phys. Fluids* **9**, 1658–1673 (1966).
- ⁵⁶D. Zhang, A. Xu, Y. Zhang, and Y. Li, “Two-fluid discrete Boltzmann model for compressible flows: based on Ellipsoidal Statistical Bhatnagar-Gross-Krook,” *Phys. Fluids* **32**, 126110 (2020).
- ⁵⁷A. J. Wagner and J. M. Yeomans, “Breakdown of Scale Invariance in the Coarsening of Phase-Separating Binary Fluids,” *Phys. Rev. Lett.* **80**, 1429–1432 (1998).
- ⁵⁸M. R. Swift, W. R. Osborn, and J. M. Yeomans, “Lattice Boltzmann Simulation of Nonideal Fluids,” *Phys. Rev. Lett.* **75**, 830–833 (1995).
- ⁵⁹V. Sofonea and K. R. Mecke, “Morphological characterization of spinodal decomposition kinetics,” *The European Physical Journal B-Condensed Matter and Complex Systems* **8**, 99–112 (1999).